

# Image Feature Assessment for Prediction of Atmospheric Optical Turbulence

Skyler Schork<sup>1</sup>, Charles Nelson<sup>2</sup>, John Burkhardt<sup>1</sup>, Cody Brownell<sup>1,\*</sup>

1: Mechanical Engineering Dept., U.S. Naval Academy, USA

2: Electrical and Computer Engineering Dept., U.S. Naval Academy, USA

\* Correspondent author: brownell@usna.edu

**Keywords:** Optical turbulence, imaging, machine learning, atmospheric surface layer

## ABSTRACT

Fluctuations of the refractive index in the atmosphere, known as optical turbulence, impact a wide variety of optical and imaging systems. These refractive index fluctuations are driven primarily by fluctuations in temperature, and are typically quantified by the refractive index structure constant  $C_n^2$ . This work uses machine learning to examine several gradient and perception-based image features with regard to their ability to estimate  $C_n^2$ , both independently and in concert with other accessible quantities.

---

## 1. Introduction

Laser propagation in the atmosphere is affected by turbulent fluctuations of the refractive index of the medium, known as optical turbulence. Optical turbulence, especially over longer propagation paths, will cause a laser beam to experience loss of coherence, excess spreading, and reduced irradiance on target. Refractive index fluctuations, driven primarily by fluctuations in temperature, are typically quantified by the refractive index structure constant  $C_n^2$ . For isotropic turbulence, this is defined as (Andrews & Phillips, 2005):

$$D(r) = \langle (n(x) - n(x+r))^2 \rangle = C_n^2 r^{\frac{2}{3}} \quad (1)$$

Where  $n$  is the refractive index,  $r$  is the separation between streamwise points in the flow, and angle brackets denote averaging. The scaling of  $D \sim r^{2/3}$  is valid within the inertial subrange for streamwise increments (Obukhov, 1970).

There are a wide variety of approaches to determining the refractive index structure constant in a given environment. Direct measurements of the medium via, e.g., sonic anemometers can yield the temperature structure function (defined analogously to the index of refraction structure parameter above) typically at a single point in the medium (Barnett et al. 2022; Peralta et al. 2021). The most straightforward method for producing  $C_n^2$  is then:

$$C_n^2 = \left( 79 \times 10^{-6} \left[ \frac{k}{\text{mbar}} \right] \frac{P}{T^2} \right)^2 C_T^2 \quad (2)$$

where  $P$  is atmospheric pressure and  $T$  is absolute temperature. This and other similar methods typically neglect secondary effects of atmospheric composition, humidity, etc. Any changes in atmospheric structure over a long propagation path are likely unknown, and prediction of optical propagation over a slant path (with changing elevation) based on a single fixed point may require a model for changes in  $C_n^2$  with altitude (Andrews et al. 2009; Hufnagel, 1974).

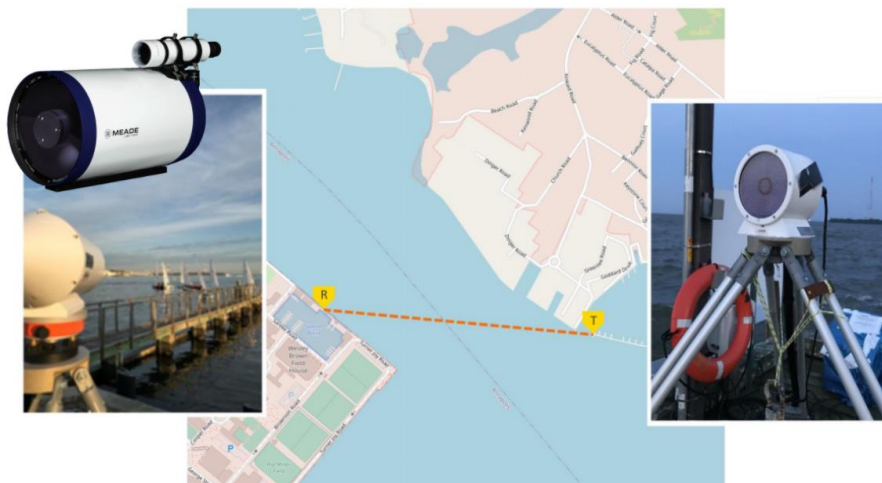
Two-sided optical methods such as a scintillometer can be used to estimate  $C_n^2$  over a known propagation path. A scintillometer will determine the path-averaged value of the refractive index structure constant via the Rytov variance, calculated from intensity fluctuations that arrive at a receiver / telescope from a known light source. As a two-sided system scintillometers cannot be easily deployed in all environments, and they can also suffer from saturation issues in strong turbulence (Kleissl, 2010).

As an alternative to scintillometry, several investigators have studied the use of imaging for determination of optical turbulence. Zamek et al. (2006) acquire video sequences and use a measure of temporal intensity fluctuations in image windows with high spatial variance. They find good agreement with scintillometer data over relatively short propagation paths. Oermann (2014) also attempts to estimate  $C_n^2$  from imagery, this time focusing primarily on spatial fluctuations of edges. They find correlations between their metric and a scintillometer of 0.81 or greater, and determine that their method is robust for both light and moderate turbulence. They also found significant anisotropy at their imaging height (approx. 1.5-m above ground), with vertical disturbances generally twice that observed in the horizontal plane. Other methods involving e.g. feature motion of distant targets (McCrae et al., 2017; Bose-Pillai et al., 2018) or curve fits to spatial spectra (Terry & O'Neill, 2014) have also been demonstrated.

The present work explores new options for assessing optical turbulence with imaging. A regression tree model has been built to assess a wide range of alternative image features to determine which elements or combination of elements can most effectively be used to predict optical turbulence. Scintillometer data from a BLS 450 serves as an independent measure of  $C_n^2$  for supervised training in all cases. The regression tree model is based on both image features and other accessible data such as time of day, range to target, etc. – much of which is available in the metadata of modern digital images.

## 2. Imaging and Image Features

Of particular interest in this investigation is low-altitude atmospheric optical turbulence in the near-maritime environment. Here, “near-maritime” is used to describe over-water optical propagation paths that retain significant terrestrial influence in flow and turbulence structure via roughness, albedo, etc. The imaging path, shown in Fig. 1, is approximately 1-km long over the mouth of the Severn River, adjacent to the Chesapeake Bay in Annapolis, MD, USA. Imaging equipment consists of a Canon EOS 5D Mark IV DSLR camera and a Meade LX85 8” telescope. Adjacent to the camera is a Scintec BLS 450 scintillometer, set up such that the camera is at the receiver end and the image FOV includes the scintillometer transmitter.



**Figure 1.** The atmospheric optical turbulence observation site at the US Naval Academy. The optical path of the scintillometer is noted in the figure. The Severn River extends out the upper left, and the Chesapeake Bay is below and to the right.

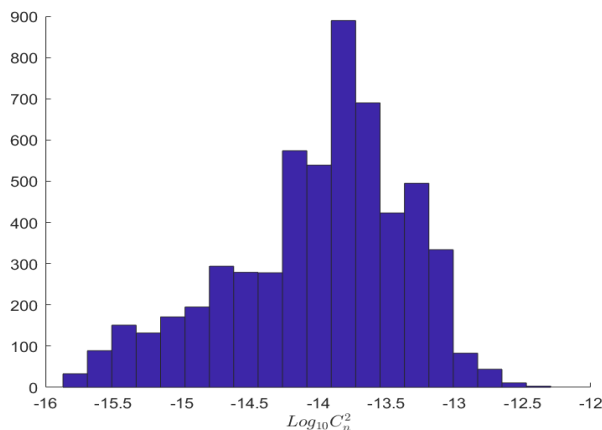
Figure 2 shows a representative image from a set of data collected in October 2021. The ships in the image are 1.1-km from the camera, and are used as a target because of their known feature dimensions and relatively high contrast with the surroundings. The complete data set of images used in this study includes over 34,000 individual exposures, captured during daylight hours between September 2021 and April 2022. Although different regions in each image correspond to different optical paths, the structure of the shoreline is such that all optical paths that are relevant to this work are predominantly over water.



**Figure 2.** Sample image from 1-km over water path.

Most prior work relating image characteristics to turbulence has examined temporal characteristics, either high-frequency intensity fluctuations or feature motion. These place restrictions on the frame rate and/or the motion of the target and acquisition system. This work seeks to explore the use of alternative image features, being those that are either gradient (sharpness) based, or perception based. These are features that may be extracted from a single frame with no reference to either target characteristics or to other image frames. The features that fit this restriction, along with other image characteristics that appear in the metadata (e.g., time of day, mean pixel intensity, etc.) are explored for use as turbulence predictors. The initial list of features considered was Sobel, Miller-Buffington, Magnitude of Gradient, and Laplacian of Gaussian as sharpness features; PIQE, NIQE, and BRISQUE as perception-based features, and mean pixel intensity, entropy, and temporal hour weight as additional features that are accessible from a single image and its metadata. Temporal hour weight (THW) is the fractional time of image capture between sunrise and sunset. While not a machine learning feature, the distance from camera to target was also used to scale the supervised value according to theory.

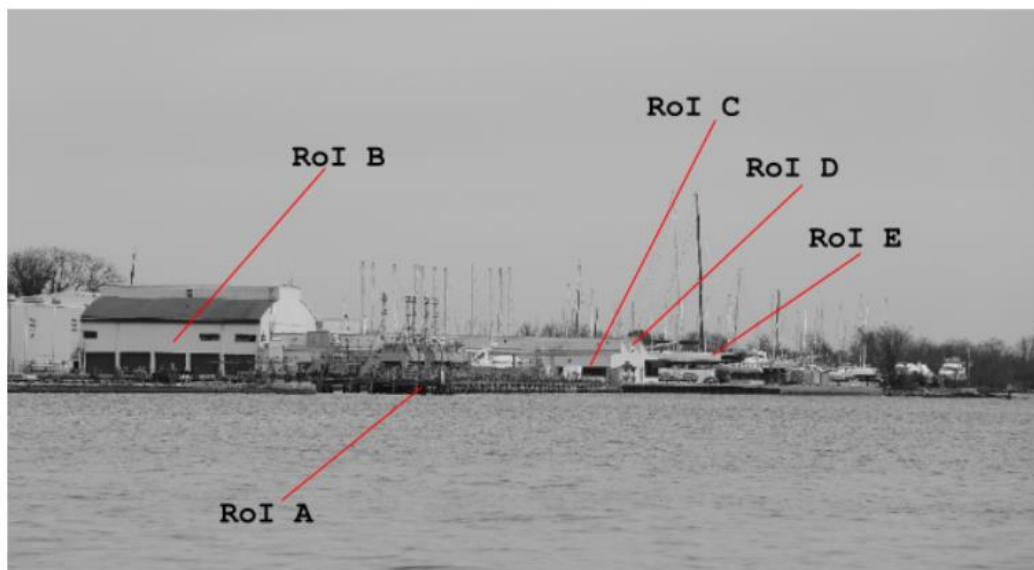
Figure 3 shows histograms of  $C_n^2$  derived from scintillometer data. Values for each are 1-minute averages, and come from a data set that was collected over approximately four days. The distributions of the optical turbulence structure parameter from the scintillometer during image acquisition match that from prior datasets acquired at this location (Jellen et al., 2020; Jellen et al., 2021). The entire data set, captured over several months, includes images acquired at various times of day and under a wider range of atmospheric conditions than what is shown in the figure.



**Figure 3.** Distribution of the refractive index structure parameter  $C_n^2$  over 96 hrs.

### 3. Data Partitioning and Optical Path

To exploit the rich information contained in image data, each image that was collected was evaluated at five different regions of interest (RoI). These five regions were selected based on their image quality assessment suitability. These criteria included regions of the original image that consisted of strong and defined edges, both horizontal and vertical features. Additionally, as these regions of interest were defined in an effort to increase the flexibility of the final model, it was important to select regions of interest that were at varying ranges from the camera. Figure 4 depicts a sample photo indicating the five RoIs.



**Figure 4.** Uncropped image highlighting all 6 regions of interest.

The regions of interest highlighted in Fig. 4 are discussed more thoroughly below in Table 1 to include an image description, the range from the camera to the region of interest as determined by satellite imagery, as well as a detailed picture of each region.

The distances between camera and RoI were used to calculate the expected Log Amplitude Variance and Fried Parameter for each propagation path. Similar to the Rytov variance, the Log Amplitude Variance,  $\sigma_\chi^2$  is given by,

$$\sigma_\chi^2 = 0.124C_n^2 k^7 L^{\frac{11}{6}} \quad (3)$$

while, for a spherical wave, the Fried Parameter,  $r_0$  is given by,

$$r_0 = \frac{3^{-3/5}}{8} (0.423C_n^2 k^2 L)^{-\frac{3}{5}}. \quad (4)$$

In Eqns (3) and (4) above,  $k$  is wavenumber and  $L$  is the optical path length. To account for the different ranges while constructing the models,  $C_n^2$  values from the scintillometer were converted to both the Fried Parameter and separately to the Log Amplitude Variance. Machine learning models using the image features from an RoI were then trained on each of the distance-dependent parameters, assuming the scintillometer's path-averaged value for  $C_n^2$  would remain constant over the other similar, neighboring optical propagation paths.

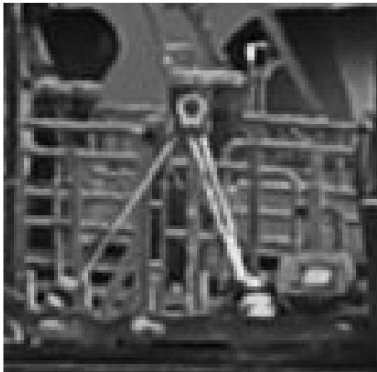

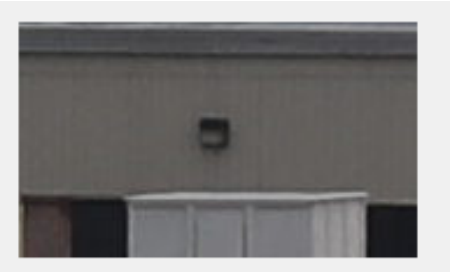
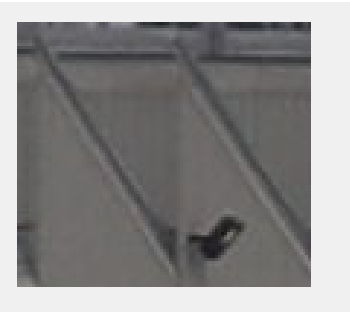

## 4. Results

Machine learning models are developed entirely from collected data and therefore allow the model to determine the significant parameters in the estimation of  $C_n^2$ . Here, one supervised linear model and three supervised ensemble models are presented. The linear model of interest is the generalized linear model, while the three ensemble models that were trained employed Bagging, Random Forest, and Boosting techniques.

### 4.1 Feature Performance

Prior to the construction of the models, the suitability of the predictor features were examined to prevent a poor predictor feature from inhibiting the strength of the developed models. In order to determine the performance of each feature, a scatterplot matrix was created to demonstrate the relationship between each of the other features. This matrix is shown in Fig. 5.

Table 1: Summary of regions of interest.

Region of Interest	Image Range [m]	Image Description	Image of Region of Interest
A	890	Scintillometer Receiver	 A black and white photograph showing a scintillometer receiver. It features a complex structure of metal beams and a central vertical component, possibly a sensor or antenna, mounted on a platform.
B	770	Big Building Wall	 A black and white photograph of a large, light-colored building wall. Two dark rectangular windows are visible, each with a small white rectangular mark or sensor positioned below it.
C	1150	Small Building Wall	 A black and white photograph of a small building wall. A single dark rectangular window is visible, with a small white rectangular mark or sensor positioned below it.
D	1180	Triangular Roof	 A black and white photograph of a triangular roof structure. The roof is supported by several beams, and a small white rectangular mark or sensor is visible on the lower part of the structure.
E	1270	Base of Yacht	 A black and white photograph showing the base of a yacht. The image is mostly dark, with a small white rectangular mark or sensor visible on the left side.

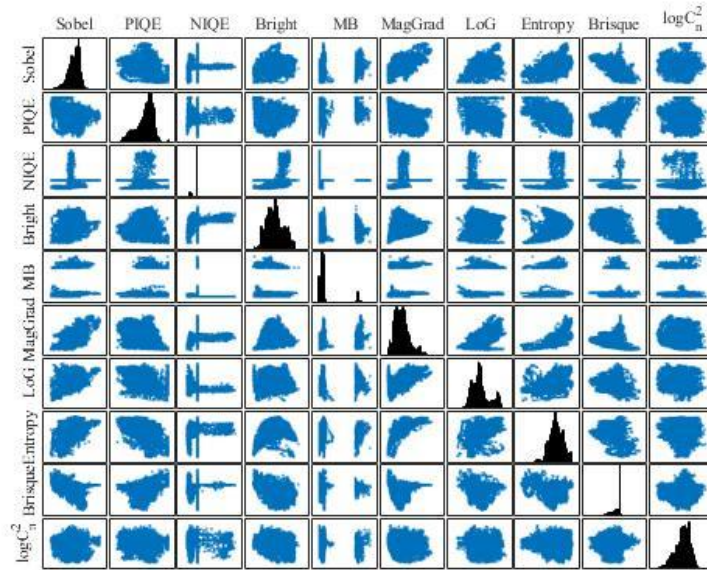


Figure 5. Scatter plot matrix for feature performance.

In Fig. 5, a random distribution is a positive result for the inclusion of both features, implying that they are uncorrelated as predictor variables. If there are relationships between features, this would indicate that one of these features would not be independent and would not be included in the final model. The histograms that populate the diagonal of the figure show the probability distribution of that variable. From this, three of the features are not well distributed in the sample. The NIQE, Miller-Buffington Sharpness, and BRISQUE features each show one or two preferred values and are unlikely to provide predictive optical turbulence information. These three features were not included when constructing the final models.

## 4.2 Linear Model

A stepwise regression is a specific kind of a multiple linear regression where terms are systematically added and removed from the model based on a certain criterion (Dobson, 1990). The reason that stepwise regression was selected for this analysis was due to the fact that there was significant uncertainty as to which, if any, features would hold the statistical significance in determining the response. The criterion most commonly used in literature for this situation is the mean square error (MSE). The MSE is defined as the following,

$$MSE = \frac{1}{n} \sum_{i=1}^n (y_i - \hat{y}(x_i))^2 \quad (5)$$

where the MSE is calculated by averaging the sum of the  $n$  observations of the squared difference between the model predicted value,  $\hat{y}(x_i)$ , and the supervised value,  $y_i$ .



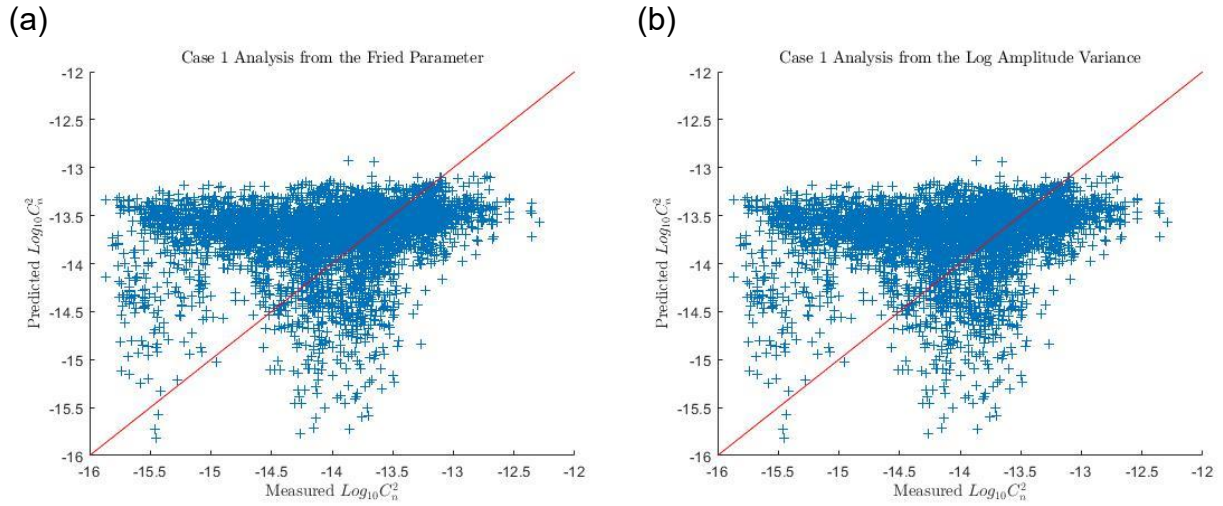
Models were built and trained on both Log Amplitude Variance and on Fried Parameter. For each of those, we considered models with and without interaction terms. When interaction terms are not allowed, there is one corresponding coefficient,  $\beta_j$ , per training feature,  $j = \{1, \dots, 7\}$ , in the  $X$  matrix. However, when interaction terms are allowed, a new coefficient,  $\beta_{jk}$ , is used to scale the new interaction predictor value,  $x_{jk} = x_j \cdot x_k$ . For simplicity, only the models with interaction terms are shown below. In order to train the generalized linear model (GLM), 80% of the data collected was categorized as the training set, while the remaining 20% was used to test the model. While the training set and the test set did not overlap, they were both composed of features from the same set of RoIs.

For the given test set, the predicted values from the generalized linear model were then converted back into  $C_n^2$  values. The resulting predicted  $C_n^2$  values calculated from the predicted Fried Parameter values are shown in Fig. 6a, and from the Log Amplitude Variance in Fig. 6b. The red line in each of the plots below is indicative of how a perfect model would perform whereby the predicted values would be equal to the measured values.

The Mean Square error was calculated for each of the models shown in Fig. 6 based off of the predicted  $C_n^2$  values and the given or measured  $C_n^2$  values. The Generalized Linear Model with interaction terms attained an MSE of 0.603 for both scenarios. Without interaction terms, model performance was similar. Consistent with the literature (Tunick, 2005; Frederickson, 2000), a review of Fig. 6 supports the conclusion that the generalized linear model failed to predict  $C_n^2$  for both cases. The GLM captured the mean value of the data set, but is generally unable to account for variations in the turbulence.

### 4.3 Bagged Regression Trees

Bagging is a technique used to mitigate variance within a dataset (Kuhn, 2013). With Bagging, separate decision trees are created off of bootstrapped copies of original data, where the final model is a combination of all the separate decision trees (James, 2013). Using the bootstrap technique, certain pockets of data are allocated to specific decision trees. This technique reduces variance among the trees by preventing the same splitting criterion at each nodal partition from dominating the decision matrix. For a set of random observations,  $n$ , the variance of the mean of the observations is given by,  $\frac{\sigma^2}{n}$ , where  $\sigma^2$  is the variance of the observations. From this relationship it becomes clear that in order to reduce the variance, we can average a set of observations. This conclusion lends itself to the discussion of statistical learning where predicted models are



**Figure 6.** (a) Stepwise generalized linear model for the Fried Parameter (with interaction terms), (b) Stepwise generalized linear model for the Log Amplitude Variance (with interaction terms)

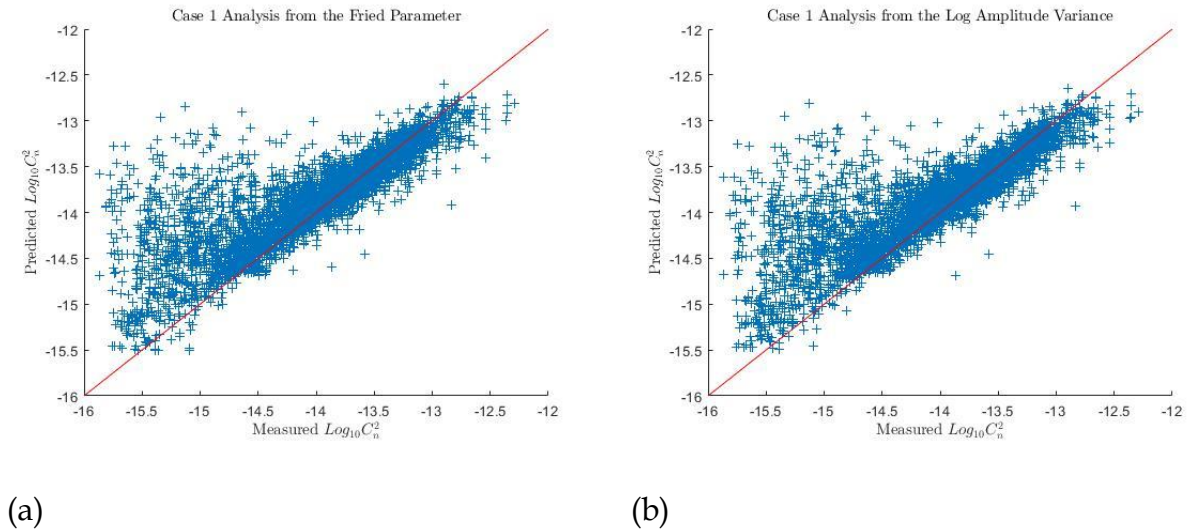
averaged to reduce variance. However, it is typically impractical to collect enough training sets to be able to construct enough separate prediction models. In order to mitigate this, a technique known as bootstrapping is often employed. Bootstrapping is a technique where multiple random samples are repeatedly drawn from the same single training data set. Bagging is the result of applying this bootstrapping technique to train a model. The bagged model is given by,

$$\widehat{f}_{bag}(x) = \frac{1}{B} \sum_{b=1}^B \widehat{f}^{*b}(x) \quad (6)$$

In order to apply bagging to a regression tree, a fixed number of trees,  $B$ , are constructed using a fixed number of random samples,  $b$ , from the training data set, and the resulting predictions are averaged.

An initial Bagged Regression Tree was constructed using the same data partitioning as with the GLM, where 80% of the data collected was categorized as the training set and the remaining 20% was used to test the model. For the given test set, the predicted Fried Parameter and Log Amplitude Variance values from these Bagged Regression Trees were then converted back into  $C_n^2$  values for analysis. The model performance is shown in Fig. 7.

As shown in Fig. 7 an initial visual analysis suggests that the Bagged Regression Tree had a higher accuracy prediction rate as compared to the generalized linear models. This is supported by the mean square error of the Bagged Regression Tree model with a value of 0.148 when trained for both the prediction of the Fried Parameter and the Log Amplitude Variance, nearly 20% of that



**Figure 7.** Bagged Regression Tree model trained to predict Fried Parameter (a) and Log Amplitude Variance (b).

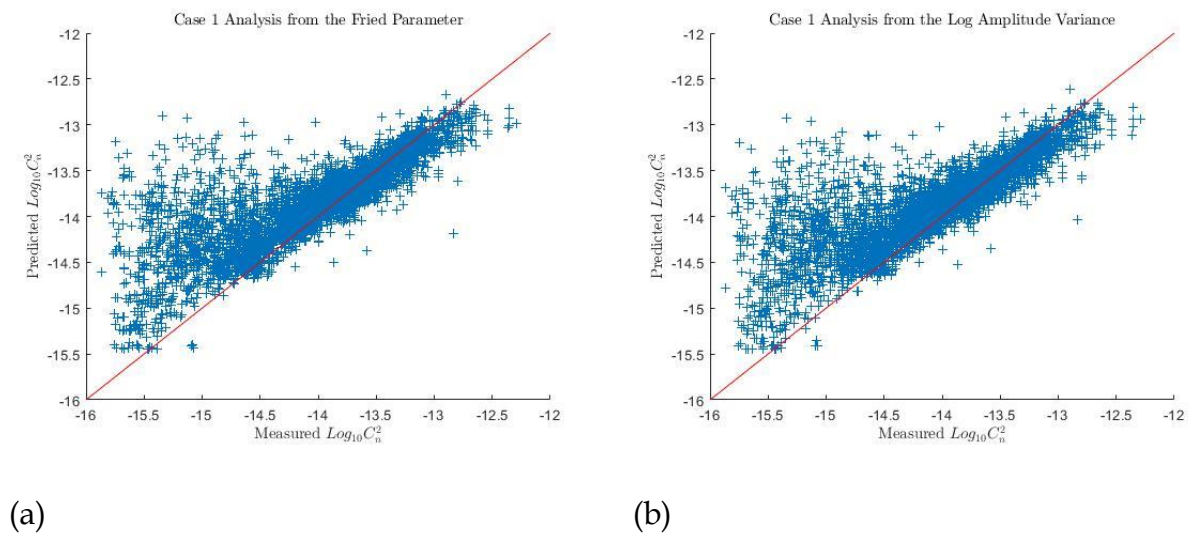
calculated for either generalized linear model. The largest errors appear to be clustered in the region generalized by over-predictions of  $C_n^2$  in low turbulence environments. This may be due to actual degradation in one of the features, e.g. image sharpness, due to fog, mechanical jitter, or other intermittent factors that appear to the model like more intense optical turbulence.

#### 4.4 Random Forest

Random Forests historically are known to outperform Bagged trees by decorrelating the trees utilized by the model (James, 2013). The process of building multiple trees trained on bootstrapped training samples is the same as in Bagging, however now, each time a split is considered in the tree, the split is selected based on a random sample of predictors. For a sample size of  $p$  predictors, a random sample of  $m$  predictors is selected. The standard practice is to take  $m \approx \sqrt{p}$ . The reason why Random Forest models are forced to select such a small random sample of predictors is to prevent one strong predictor in the data set from dominating the formation of the trees. In bagging, a strong predictor has the potential to drive the construction of all of the trees since this random sample is not allocated, and as a result many of the trees end up with stark similarities. Random Forest models use this random sample in order to decorrelate trees as on average  $(p - m)/p$  of the potential splits in the random sample do not include the strongest identified predictor. Ultimately the Random Forest model differs from the Bagged Regression Tree in regards to the size of  $m$ . When Bagging is employed, all of the predictors are considered at the nodal partition. Mathematically this is the equivalent of stating that in Bagging the number of predictors considered,  $m$ , was equal to the total number of predictors,  $p$ . In a Random Forest model,  $m$ , is a

random sample taken from  $p$ , and  $m \approx \sqrt{p}$ , in and in Bagging,  $m = p$ . The results for the Random Forest models are shown below in Fig. 8. For the given test set, the predicted Fried Parameter and Log Amplitude Variance values from these Random Forest Models were converted back into  $C_n^2$  values for analysis.

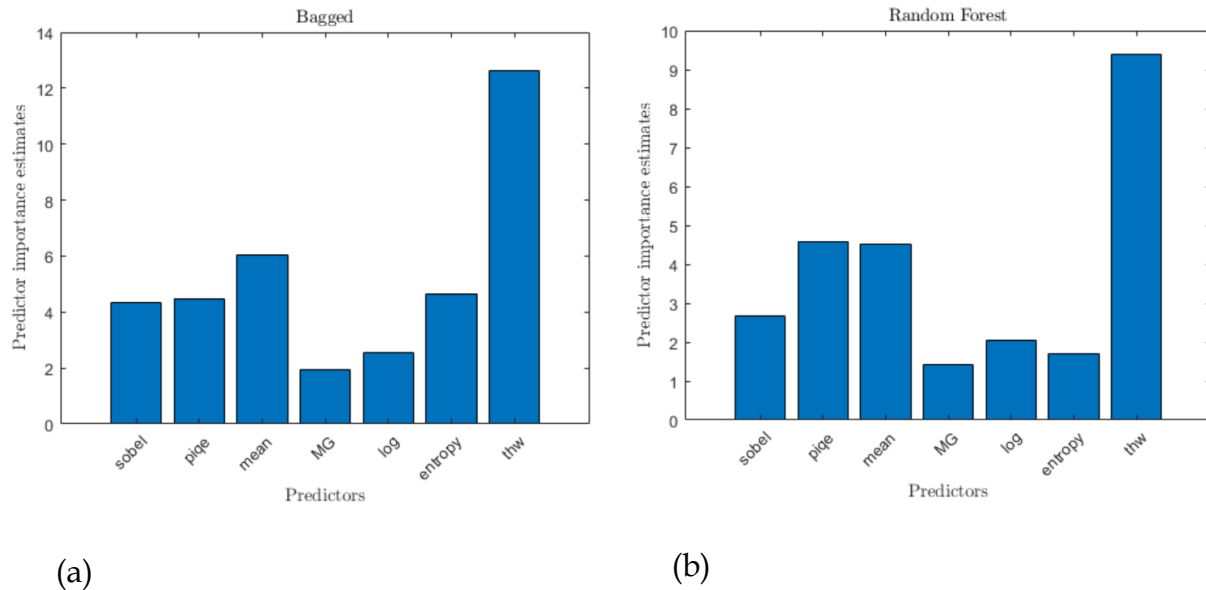
As shown in Fig. 8 an initial visual analysis suggests that the Random Forest Model performed similarly to the Bagged Regression Tree while highly outperforming the generalized linear models. This is supported by the mean square error of the Random Forest model with a value of 0.1686 when trained for the prediction of the Fried Parameter as compared to the 0.568 MSE by the generalized linear model with interaction terms trained for the prediction of the Fried Parameter. However, the MSE for the Random Forest model is approximately 13.3% higher than that obtained by the Bagged Regression Tree model.



**Figure 8.** Random Forest model trained to predict Fried Parameter (a) and Log Amplitude Variance (b).

Figure 9 below shows the predictor importance plot for the Bagged Regression Tree on the left, and the predictor importance plot for the Random Forest model on the right. As applied to this research, with seven predictors, an approximate of three predictors were evaluated at each split for the Random Forest model. Fig. 9 supports the conclusion that temporal hour weight is the strongest predictor of  $C_n^2$  when either Bagging or Random Forest algorithms were employed. However, as can be seen in the figure, the importance weighting for the THW predictor decreased from approximately 12.5 for bagging to less than 10 in the Random Forest Model. This observation supports the conclusion that electing to build a Random Forest model does play a role in inhibiting the ability of the THW predictor from dominating the creation of the trees. This also prevents a

lack of variance among the trees as,  $(p - m)/p$  or approximately 62.5% of the random samples in the Random Forest model did not even consider THW as a potential split.



**Figure 9.** Predictor importance plot for the Bagged Regression Tree (a) and the Random Forest model (b).

## 4.5 Boosted Trees

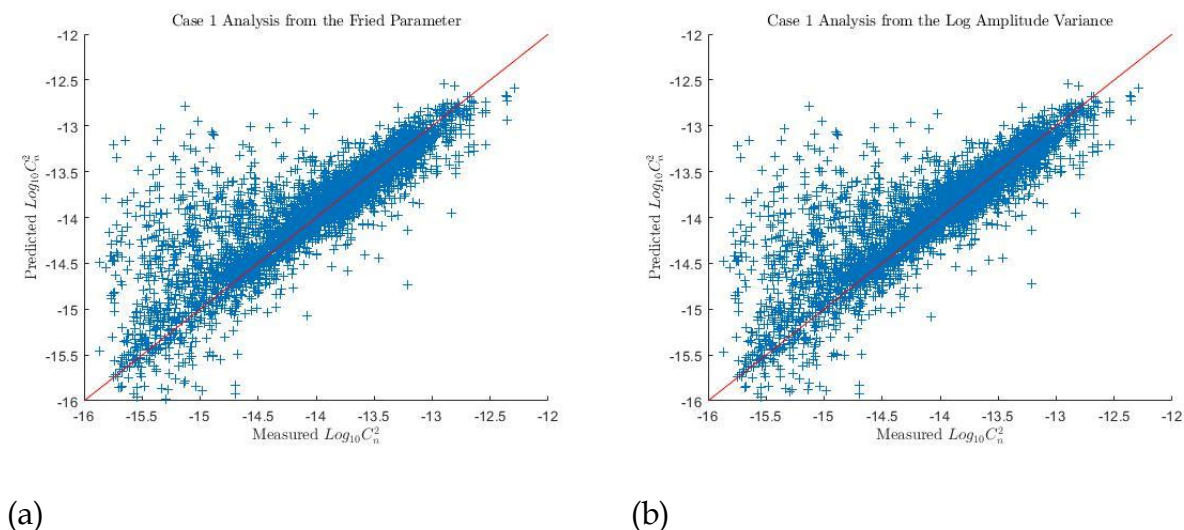
Boosted decision trees are the final method that were employed in this research, and served as another way to improve predictions from our decision trees. While employing the Bagging technique, trees were grown independently from bootstrapped samples of the overall data set. Conversely while employing the Boosting technique, the trees were created sequentially.

The sequential building technique allowed information from previous trees to dictate how and in what manner new trees were grown. Therefore, the samples of the overall data set from which boosted trees were taken from are not bootstrapped samples, but rather slightly altered versions of the original data set that were not random in nature.

The first step in the algorithm was to set the predicted response,  $\hat{y}(x)$  equal to zero, as well as set the residuals equal to the predicted response for each of the predictors in the data set. Each of the subsequent trees,  $b = 1, 2, 3 \dots B$ , were built using the residuals,  $r$ , rather than the predicted response. The predicted response was updated after adding a version of a new tree modified with the shrinkage parameter,  $\lambda$ , and the residuals were updated. The shrinkage parameter dictated the learn-rate of the boosting model ranging from small positive value of 0.001 to 0.01. The literature suggests that the learning rate and the number of trees are inversely related such that a small

learning rate may require a larger number of trees to improve accuracy (Jellen, 2022). The results for the Boosted regression models are shown below in Fig. 10.

The Boosted regression tree performed well when compared to both the Bagged Regression Tree and the Random Forest model, while also outperforming the generalized linear models. The mean square error of the Boosted regression tree model with a value of 0.134 when trained for the prediction of the Fried Parameter; this was the smallest out of all of the models tested.



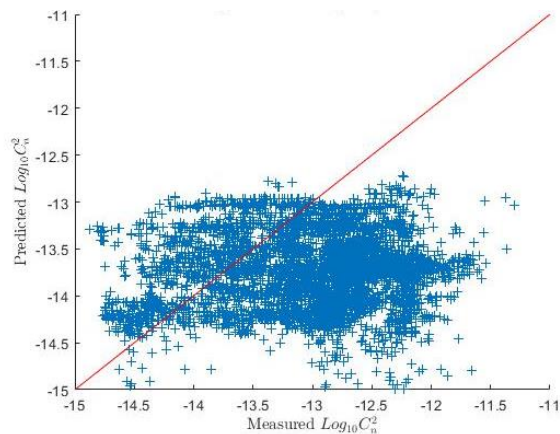
**Figure 10.** Boosted regression tree model trained to predict Fried Parameter (a) and Log Amplitude Variance (b).

## 4.6 Generalizability

In each of the above models, the training data and test data were drawn from the same RoIs. To understand the generalizability of an image-based model for predicting optical turbulence, we require predictive capabilities when operating with image regions that have not been part of any training set. To explore this, the Boosted regression tree was trained to predict the Log Amplitude Variance for several cases where the training and test data were taken from different RoIs. Case 1 refers to the previous results with overlapping RoI. Case 2 and Case 3 both refer to models trained on four of the RoIs, and then tested on the fifth RoI that would be new to the model. The test RoI for Case 2 is RoI A and for Case 3 is RoI D. The results of these tests are shown in Fig. 11 below. The analysis shown below illustrates the model's accuracy in determining  $C_n^2$  values calculated from the model's predictions for the Fried Parameter and the Log Amplitude Variance. Both of these models were unable to predict  $C_n^2$ , displaying larger MSE than even the GLM when provided with overlapping data regions. This finding raises significant questions as to the

generalizability of one-sided sharpness and perception based imaging methods for prediction of optical turbulence.

Case 2 - MSE 1.23



Case 3 - MSE 1.14

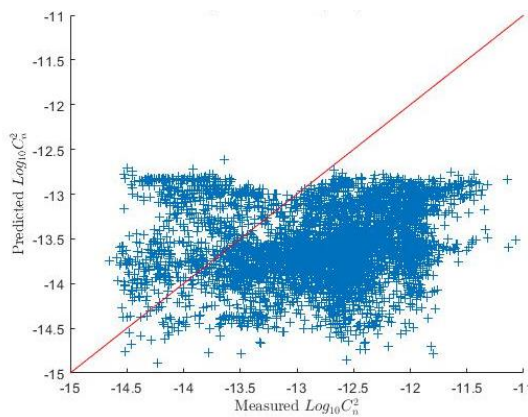


Figure 11. Cases 2-3 evaluated for the Boosted regression tree model, with separate RoIs for training and test.

## 5. Conclusions

From a set of images, we were able to extract features that then enabled us to determine the strength of optical turbulence quantified by  $C_n^2$ . In order to achieve this, machine learning techniques were employed with a set of specific image quality metrics as features. While a host of candidate learning features were evaluated for their effectiveness and independence, the seven final features included in the models were the Image Gradient sharpness, Entropy, PIQE, Mean Intensity, Laplacian of Gaussian, Sobel, and Temporal Hour Weight. Through a feature performance exercise, the Miller-Buffington sharpness feature as well as NIQE and BRISQUE were removed from the feature slate due to their inability to scale their outputs for varying  $C_n^2$  inputs.

The success of the Case 1 structured models with overlapping RoIs was juxtaposed with the performance of the Case 2-3 structured models where the models were tested on a new, unseen RoI. This analysis demonstrated the lack of generalization exhibited by the models. This inability to effectively generalize supports the conclusion that the model performs extremely well when fed images from familiar RoIs or of familiar subjects, however it struggles when unknown regions are presented. It is possible that an expanded data set would yield improved results for Cases 2 and 3. However, future exploration of this type of technique perhaps should focus on features most likely to be present in near-maritime operating environments such as bridges and buildings - these may produce adequate predictions, even in cases where linear models have failed in the past.

## Acknowledgements

The authors are grateful for support from the ONR Code 35 and DE-JTO.

## References

- Andrews, L. C., & Phillips, R. L. (2005). Laser beam propagation through random media. *Laser Beam Propagation Through Random Media: Second Edition*.
- Andrews, L. C., Phillips, R. L., Wayne, D., Leclerc, T., Sauer, P., Crabbs, R., & Kiriazes, J. (2009, April). Near-ground vertical profile of refractive-index fluctuations. In *Atmospheric Propagation VI* (Vol. 7324, p. 732402). International Society for Optics and Photonics.
- Barnett, S., Blau, J., Frederickson, P., & Cohn, K. (2022). Measurements and Modeling of Optical Turbulence in the Coastal Environment. *Applied Sciences*, 12(10), 4892.
- Bose-Pillai, S. R., McCrae, J. E., Rice, C. A., Wood, R. A., Murphy, C. E., & Fiorino, S. T. (2018). Estimation of atmospheric turbulence using differential motion of extended features in time-lapse imagery. *Optical Engineering*, 57(10), 104108.
- Frederickson, P. A., Davidson, K. L., Zeisse, C. R., & Bendall, C. S. (2000). Estimating the refractive index structure parameter ( $\chi^2$ ) over the ocean using bulk methods. *Journal of applied meteorology*, 39(10), 1770-1783.
- Google Earth. (n.d.). Google. Retrieved April 1, 2022, from <https://earth.google.com/web>
- Hufnagel, R. E. (1974, July). Variations of atmospheric turbulence. Digest of technical papers. In *Topical meeting on optical propagation through turbulence*, University of Colorado, Boulder, CO.
- James, G., Witten, D., Hastie, T., & Tibshirani, R. (2013). *An introduction to statistical learning* (Vol. 112, p. 18). New York: springer.
- Jellen, C., Burkhardt, J., Brownell, C., & Nelson, C. (2020). Machine learning informed predictor importance measures of environmental parameters in maritime optical turbulence. *Applied Optics*, 59(21), 6379-6389.
- Jellen, C., Nelson, C., Brownell, C., Burkhardt, J., & Oakley, M. (2020). Measurement and analysis of atmospheric optical turbulence in a near-maritime environment. *IOP SciNotes*, 1(2), 024006.
- Jellen, C., Oakley, M., Nelson, C., Burkhardt, J., & Brownell, C. (2021). Machine-learning informed macro-meteorological models for the near-maritime environment. *Applied Optics*, 60(11), 2938-2951.



- Kleissl, J., Hartogensis, O. K., & Gomez, J. D. (2010). Test of scintillometer saturation correction methods using field experimental data. *Boundary-layer meteorology*, 137(3), 493-507.
- Kuhn, M., & Johnson, K. (2013). *Applied predictive modeling* (Vol. 26, p. 13). New York: Springer.
- Li, D., Bou-Zeid, E., & De Bruin, H. A. (2012). Monin-Obukhov similarity functions for the structure parameters of temperature and humidity. *Boundary-layer meteorology*, 145(1), 45-67.
- McCrae, J. E., Bose-Pillai, S. R., & Fiorino, S. T. (2017). Estimation of turbulence from time-lapse imagery. *Optical Engineering*, 56(7), 071504.
- Obukhov, A. M. (1970). *Structure of temperature field in turbulent flow*. AIR FORCE SYSTEMS COMMAND WRIGHT-PATTERSON AFB OH FOREIGN TECHNOLOGY DIVISION.
- Oermann, R. J. (2014). *Novel methods for the quantification of atmospheric turbulence strength in the atmospheric surface layer* (Doctoral dissertation).
- Peralta, A. M., Nelson, C., & Brownell, C. J. (2021). Characterization of Atmospheric Optical Turbulence Using Turbulence Flux Measurements. *Proceedings of the 23rd Directed Energy Science and Technology Symposium*. (Virtual).
- Terry, D. D., & O'Neill, M. D. (2014). *Passive method to characterize atmospheric turbulence* (No. DOE/NV/25946-2179). Nevada Test Site/National Security Technologies, LLC (United States).
- Tunick, A., Tikhonov, N., Vorontsov, M., & Carhart, G. (2005). *Characterization of optical turbulence (Cn2) data measured at the ARL A\_LOT facility*. US Army Research Laboratory Adelphi United States.
- Wyngaard, J. C., Izumi, Y., & Collins, S. A. (1971). Behavior of the refractive-index-structure parameter near the ground. *JOSA*, 61(12), 1646-1650.
- Zamek, S., & Yitzhaky, Y. (2006). Turbulence strength estimation from an arbitrary set of atmospherically degraded images. *JOSA A*, 23(12), 3106-3113.